ACSNANO

www.acsnano.org

ARTICLE

A Comparative Study of Ultrasmall Calcium Carbonate Nanoparticles for Targeting and Imaging Atherosclerotic Plaque

Lydia Martínez-Parra,[%] Marina Piñol-Cancer,[%] Carlos Sanchez-Cano, Ana B. Miguel-Coello, Desirè Di Silvio, Ana M. Gomez, Clara Uriel, Sandra Plaza-García, Marta Gallego, Raquel Pazos, Hugo Groult, Marc Jeannin, Kalotina Geraki, Laura Fernández-Méndez, Ainhize Urkola-Arsuaga, María Jesús Sánchez-Guisado, Juliana Carrillo-Romero, Wolfgang J. Parak, Maurizio Prato, Fernando Herranz, Jesús Ruiz-Cabello,* and Susana Carregal-Romero*

Cite This: *ACS Nano* 2023, 17, 13811−13825

Read Online

ACCESS | Metrics & More | Article Recommendations | Supporting Information

ABSTRACT: **Atherosclerosis is a complex disease that can lead to life-threatening events, such as myocardial infarction and ischemic stroke. Despite the severity of this disease, diagnosing plaque vulnerability remains challenging due to the lack of effective diagnostic tools. Conventional diagnostic protocols lack specificity and fail to predict the type of atherosclerotic lesion and the risk of plaque rupture. To address this issue, technologies are emerging, such as noninvasive medical imaging of atherosclerotic plaque with customized nanotechnological solutions. Modulating the biological interactions and contrast of nanoparticles in various imaging techniques, including magnetic resonance imaging, is possible through the careful design of their physicochemical properties. However, few examples of comparative studies between nanoparticles targeting different hallmarks of atherosclerosis exist to provide information about the plaque development stage. Our work demonstrates that Gd (III)-doped amorphous calcium carbonate nanoparticles are an effective tool for these comparative studies due to their high magnetic resonance contrast and physicochemical properties. In an animal model of atherosclerosis, we compare the imaging performance of three types of nanoparticles: bare amorphous calcium carbonate and those functionalized with the ligands alendronate (for microcalcification targeting) and trimannose (for inflammation targeting). Our study provides useful insights into ligand-mediated targeted imaging of atherosclerosis through a combination of *in vivo* imaging, *ex vivo* tissue analysis, and *in vitro* targeting experiments.**

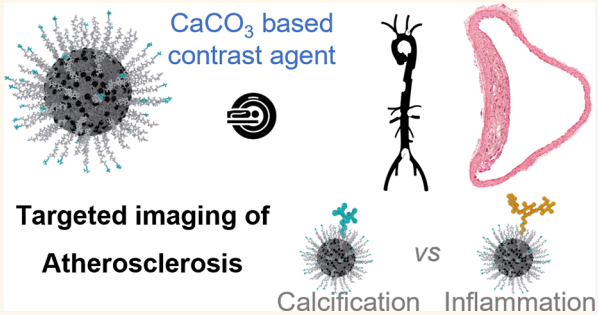

KEYWORDS: *atherosclerosis, ligand-mediated targeted imaging, amorphous calcium carbonate nanoparticles, magnetic resonance imaging, synchrotron X-ray fluorescence tissue analysis*

1. INTRODUCTION

Atherosclerosis is a chronic inflammatory disease and the main cause of most coronary heart pathologies, which are among the leading causes of death worldwide.[1] This disease is characterized by the formation of plaques in the walls of arteries, composed of fat, cholesterol, necrotic cells, calcifications, and other substances.[2] These plaques can cause aberrant blood flow and weaken the artery wall, leading to both cardiovascular diseases and possible rupture of the arteries.[3] One of the biggest challenges in managing this disease is the lack of tools for its early diagnosis and determination of plaque vulnerability, often resulting in the detection after infarction. Therefore, novel clinical diagnostic tools are needed to reduce mortality rates. Medical imaging is the gold standard for noninvasive examination of patients, and nanotechnology is regarded as a promising approach for designing smart contrast agents against atherosclerosis.[4,5]

Received: April 19, 2023
Accepted: June 27, 2023
Published: July 3, 2023

https://doi.org/10.1021/acsnano.3c03523
ACS Nano 2023, 17, 13811−13825

Nanoparticles (NPs) can provide enhanced contrast in many different imaging techniques, including magnetic resonance imaging (MRI),[6] fluorescence imaging,[7] positron emission tomography (PET),[8] or computed tomography (CT).[9] While there is consensus that MRI and PET are the most practical and comprehensive methods for imaging the plaque *in vivo*,[4,10] the lack of specificity of NP accumulation in most proposed contrast agents remains a challenge for early and plaque vulnerability diagnosis.[11−13] Different preclinical models of atherosclerosis have confirmed the unspecific accumulation of liposomes and poly(lactic-*co*-glycolic acid) (PLGA) NPs in the plaque.[11,13] To develop advanced clinical diagnostic tools, specific accumulation of nanoparticles only in the presence of disease-specific hallmarks indicating the type of atherosclerotic lesion (e.g., intimal thickening, fibroatheroma, plaque erosion) is required.[14] Targeted imaging with NPs offers a promising approach to reveal processes such as the enlargement of the necrotic core, the presence of microcalcifications, or the reduction of the fibrotic cap.[10,15,16] As a result, much scientific effort is focused on the development of targeted NP imaging for atherosclerosis.

To date, strategies such as ligand-mediated targeting and the use of biomimetic nanoparticle coatings have been applied to image atherosclerotic hallmarks.[12,16] However, most of these pioneering nanostructures have remained at the preclinical stage due to different drawbacks such as insufficient targeting efficiency or contrast.[10] The practical feasibility of nanotechnology still needs to be determined in assays comparing different parameters such as ligand type, targeted tags, and time-dependent accumulation.[10] Furthermore, these assays should take into account the sustainable and scalable production of NPs and their biosafety. Otherwise, the transformation of these technologies into clinical settings will be doomed to a dead end.[17]

In this work, we propose the use of advanced MRI contrast agents based on ultrasmall amorphous calcium carbonate (CC) NPs doped with gadolinium (Gd) as a robust and safe nanotool for comparative studies of targeted imaging in atherosclerosis. In nature, amorphous CC NPs are precursors in the formation of biogenic calcium carbonate, a major component of rocks, skeletons, or shells.[18,19] Recent interest in creating bioinspired materials has provided protocols for the large-scale synthesis of these transient NPs, ensuring good biocompatibility and colloidal stability by trapping different polyacids such as poly(acrylic acid) (PAA) and citric acid.[18,20−22] Interestingly, these polyacids act as chelating agents for Gd(III) ions, providing a highly hydrated nanoenvironment that considerably increases their longitudinal magnetic relaxivity, resulting in an unusual increase of contrast in MRI. Gd-doped amorphous CC NPs have been successfully applied for *in vivo* studies of NP biodistribution and contrast-enhanced MR angiography.[22,23]

In this study, we demonstrate these contrast agents' application in targeted atherosclerosis imaging. First, we synthesized amorphous calcium carbonate NPs with enhanced MRI contrast using a fast and cost-efficient method. We then covalently bound two types of ligands to these CC NPs for targeting microcalcifications using alendronate and inflammation through trimannose ligands. We compared the performance of the three NPs (bare and with the two ligands) for imaging the atherosclerotic plaque of LDLr−/− mice using MRI. To gain a deeper understanding of fundamental aspects of NP targeted imaging, we completed our study with synchrotron X-ray fluorescence (SXRF) analysis of arterial tissue. This technique provided elemental information on the targeted plaques and NP location in the aortic tissue,[24] revealing different behaviors in the temporal accumulation of NPs functionalized with different ligands. Our study provides insights into the field of targeted imaging of atherosclerosis and demonstrates the potential of advanced MRI contrast agents based on Gd-doped amorphous CC NPs for use as a safe and effective tool in comparative studies of targeted imaging.

2. RESULTS AND DISCUSSION

2.1. Synthesis and Characterization of MRI Nanoprobes for Targeted Imaging of Atherosclerosis. We synthesized different functional MR nanoprobes, as shown in Scheme 1a. Gd^{3+} doped ultrasmall CC NPs were prepared for

Scheme 1. (a) Schematic Illustration of the Synthesis Protocol of CC-Aln and CC-Trm. (b) Illustration of the Ligand-Mediated Accumulation of CC-Aln and CC-Trm in Atherosclerotic Plaques *via* High Affinity Binding to Calcifications and Macrophages, Respectively

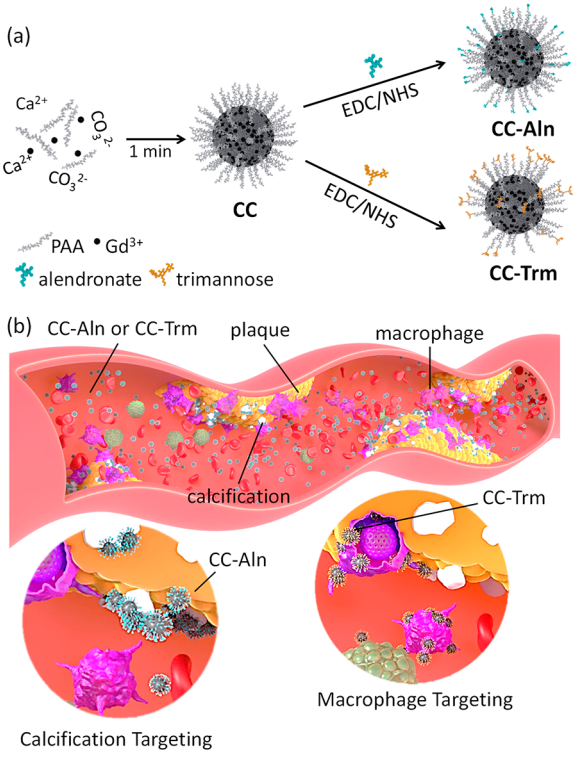

ligand-mediated imaging of either calcifications or macrophage presence (see Scheme 1b) using a two-step protocol and amino terminated ligands described in Figures S1−S8. First, we prepared Gd-doped CC NPs by mixing $CaCl_2$, $GdCl_3{\cdot}6H_2O$, PAA and Na_2CO_3 at room temperature for 1 min and then stopping the particle growth with the addition of ethanol to the reaction solution, as reported previously.[23] We separated the unreacted species from the nanoparticles by precipitation and filtration (3 kDa molecular weight cutoff) and freeze-dried the CC NPs for further use, obtaining 2.2 g of nanoparticles with a 3 wt % of Gd. The size of these NPs was 2−3 nm, as shown in atomic force microscopy (AFM), transmission electron microscopy (TEM) and scanning transmission electron microscopy (STEM) images in Figure 1a and Figure S9. Next, we covalently bound the two different ligands with amino-terminal domains, alendronate and trimannose, to the surface of

https://doi.org/10.1021/acsnano.3c03523
ACS Nano 2023, 17, 13811−13825

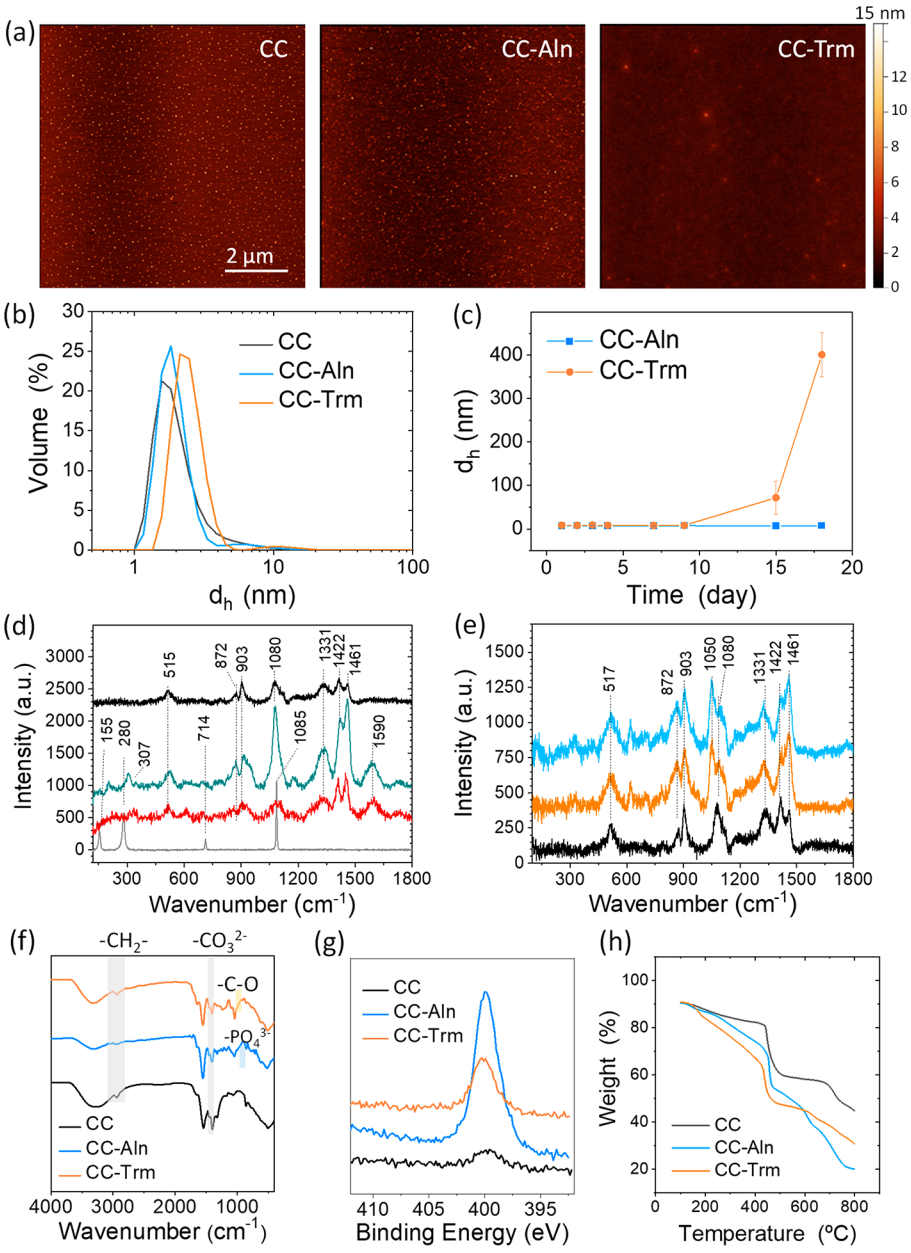

Figure 1. Characterization of targeted CC nanoprobes. (a) AFM images of Gd-doped amorphous CC NPs before and after Aln and Trm functionalization. The scale color corresponds to the NP height measured in tapping mode. (b) Hydrodynamic diameter (d_h) measurements of the three NPs. (c) Time-dependent d_h of CC-Aln and CC-Trm NPs at physiological pH 7.4 in PBS buffer. (d) μ-Raman spectra recorded at a 532 nm excitation wavelength of calcite (gray), PAA (red), undoped CC NPs (green), and Gd-doped CC NPs (black). (e) μ-Raman spectra of Gd-doped CC NPs (black), CC-Aln NPs (blue), and CC-Trm NPs (orange) (f) FT-IR spectra of CC, CC-Aln and CC-Trm NPs. (g) Core-level XPS spectra of N 1s. (h) TGA of sample powders with a heating rate of 10 °C min^{-1}.

the CC NPs via 1-ethyl-3-(3-(dimethylamino)propyl)-carbodiimide (EDC) chemistry (Scheme 1a). We extensively described the synthesis of customized amino-terminated branched trimannoside in the Supporting Information, as shown in Figures S1−S7 and Scheme S1. Alendronate (Aln) is a bisphosphonate ligand that binds hydroxyapatite (HAP, $Ca_5(PO_4)_3(OH)$) (Figure S8), which is the main component of the calcifications found in the atherosclerotic plaque. In contrast, functionalization with trimannose (Trm) targets mannose receptors highly expressed in pro-atherosclerotic macrophage subtypes located in the fibrous cap,[25,26] which are present in the plaque due to the inflammation of the artery, as illustrated in Scheme 1b.[27]

After ligand conjugation, we characterized the various CC NPs using different techniques. First, we determined the number of ligands per weight of NPs using the Rouser method for phosphorus determination (Aln) and liquid chromatography−mass spectrometry (Trm).[28] The number of Aln and Trm bound to 1 mg of CC NPs was 0.14 ± 0.01 and 0.04 ± 0.01 μmol, respectively, which corresponds approximately to 1 mannose unit per molecule of Aln. Furthermore, we calculated the weight percentage of Gd in each type of nanoprobe using inductively coupled plasma mass spectrometry (ICP-MS) and found it to be 3 wt % in all of them.

To assess the stability of the ligand-functionalized CC NPs, we compared their size with that of bare CC NPs using AFM as

https://doi.org/10.1021/acsnano.3c03523
ACS Nano 2023, 17, 13811−13825

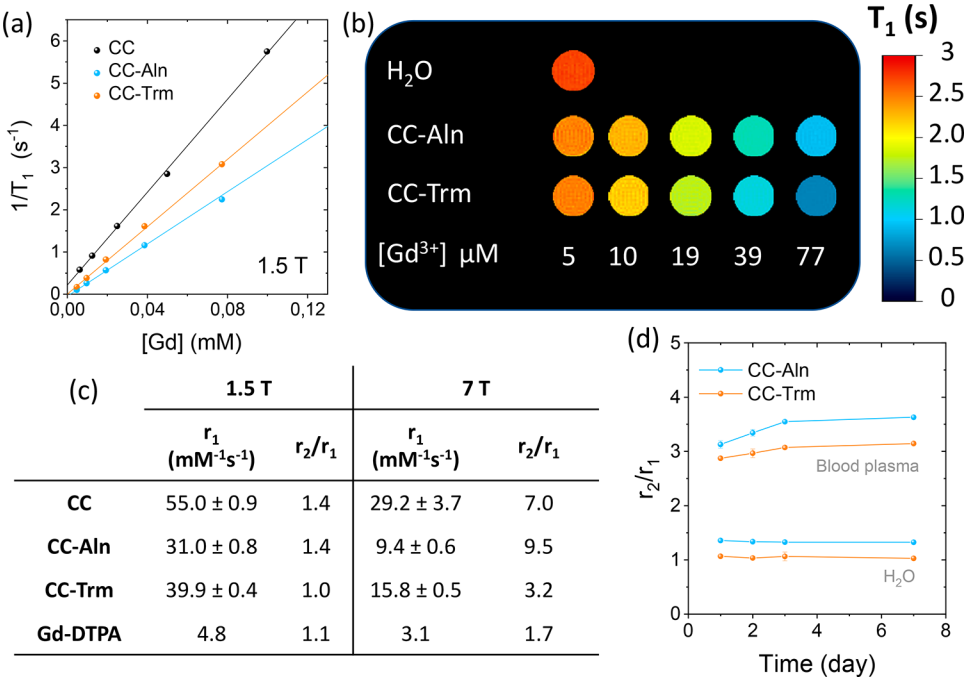

(c)

	1.5 T		7 T	
	r_1 ($mM^{-1}s^{-1}$)	r_2/r_1	r_1 ($mM^{-1}s^{-1}$)	r_2/r_1
CC	55.0 ± 0.9	1.4	29.2 ± 3.7	7.0
CC-Aln	31.0 ± 0.8	1.4	9.4 ± 0.6	9.5
CC-Trm	39.9 ± 0.4	1.0	15.8 ± 0.5	3.2
Gd-DTPA	4.8	1.1	3.1	1.7

Figure 2. MR contrast of targeted CC NPs. (a) Plot of $1/T_1$ versus Gd concentration for CC, CC-Aln and CC-Trm NPs at 1.5 T (n = 3). (b) Concentration dependence of the T_1 contrast obtained in an MRI scanner at 7 T. (c) Table of longitudinal relaxivity (r_1) data and ratio r_2/r_1 of the different nanoprobes at 1.5 and 7 T. Longitudinal stability of the relaxometric properties in different water and blood plasma (d).

shown in Figure 1a. The three types of NPs were dispersed on a mica substrate, and height (h) measurements *via* tapping mode were performed. Due to the quasi-spherical shape of NPs, it was possible to compare the obtained NP height with the NP diameter obtained with other techniques such as TEM. The results indicated a slight increase in size due to the presence of the ligands between CC and CC-Aln or CC-Trm NPs: CC (h = 2.3 ± 0.3 nm), CC-Aln (h = 3.7 ± 2.4 nm) and CC-Trm (h = 6.6 ± 1.8 nm). This shift was confirmed by measuring the hydrodynamic diameter (d_h) through dynamic light scattering (DLS), as shown in Figure 1b. Colloidal stability was ensured for at least 8 days after ligand functionalization, as shown in Figure 1c, but it was not possible to freeze-dry the samples for long-term storage, unlike the CC NPs.

The composition and structural stability of the different nanoparticles were confirmed by micro-Raman (μ-Raman) spectroscopy, Fourier transform infrared spectroscopy (FT-IR), X-ray photoelectron spectroscopy (XPS), and thermogravimetric analysis (TGA). μ-Raman spectrometry recorded at a 532 nm excitation wavelength was used to evaluate the stability of the ligand-functionalized CC NPs and confirm their composition. The Raman spectra of Gd-doped CC NPs, undoped CC NPs, PAA, and calcite (the most stable polymorph of $CaCO_3$) were compared in Figure 1d. The Gd-doped CC-NPs exhibited the typical sharp peak of amorphous calcium carbonate at 1080 cm^{-1}, which corresponds to the symmetric CO_3^{2-} stretching mode ν_1, with a slight shift when compared with the spectrum of pure calcite.[29] The spectrum also revealed a high proportion of the PAA organic coating bound to the Na^+ cations. However, the typical peaks at lower wavelengths of calcite from the ν_4-asymmetric internal stretching mode at 714 cm^{-1} and the lattice mode of the calcite at 155 and 280 cm^{-1} were not observed.[30] Similarly, no peaks typical of other polymorphs such as vaterite appear at 1090, 749, or 299 cm^{-1}, indicating that the Gd-doped CC-NPs are in the amorphous phase.[29] The PAA vibration modes at 1590 cm^{-1} (ν-asymmetric COO^-, carbonyl group), 1461 cm^{-1} (CH_2 deformation), 1422 cm^{-1} (ν-symmetric COO^-), 1331 cm^{-1} (CH_2 twist), 903 cm^{-1} (C−COO^- stretch) and 872 cm^{-1} (C−COO^- stretch), and 515 cm^{-1} (CCO bending) were clearly detected in the CC NP spectrum (with and without Gd^{3+} doping).[31,32] The higher ratio between 872 and 903 cm^{-1} peaks intensity may be indicating the presence of PAA bound to Ca^{2+} cations.[31] Samples of CC-NPs incorporating Gd^{3+} led to a similar spectra than the one of nondoped CC-NPs, except that the asymmetric CO salt peak at 1590 cm^{-1} vanished suggesting an interaction between the carbonyl groups and the gadolinium ions. The spectra of bare Gd doped CC NPs compared with their corresponding Aln and Trm coated analogs are shown in Figure 1e, which indicated that the amorphous structure was maintained. However, new peaks appeared in the Raman spectra (at 325, 411, 619, 680, and 786 cm^{-1}, etc.) that could not be unequivocally associated with their corresponding ligand. FT-IR spectra (Figure 1f) further confirmed the presence of PAA and the amorphous structure in all three CC, CC-Aln and CC-Trm NPs. Shoulders at 2942 and 1714 cm^{-1} were associated with the stretching modes of − CH_2− and − COO^- groups, indicative of the PAA presence. The split bands at 1415 and 1454 cm^{-1} in the three spectra were assigned to the asymmetric stretching vibration of carbonate ions in amorphous structures.[22,23] In addition, the phosphate group of alendronate was visible at 1050 cm^{-1} in the CC-Aln sample and the peak at 1200 cm^{-1} in the sample CC-Trm could be assigned to the −C−O groups of Trm.[33] Figure S10 provides the FT-IR spectra of Aln and Trm. XPS analysis confirmed the presence of Gd, carbonate, and carboxylic groups in the three samples (Figure S11 and Table S1). The elemental analysis of the N 1s core level showed the presence of amino terminated ligands Aln and Trm in the CC-Aln and CC-Trm NPs (Figure 1g). Finally, TGA data (Figure 1h) showed a loss of around 16 wt % upon heating to 230 °C (CC 15%, CC-Aln 15%, and CC-Trm 17%) due to the

https://doi.org/10.1021/acsnano.3c03523
ACS Nano 2023, 17, 13811−13825

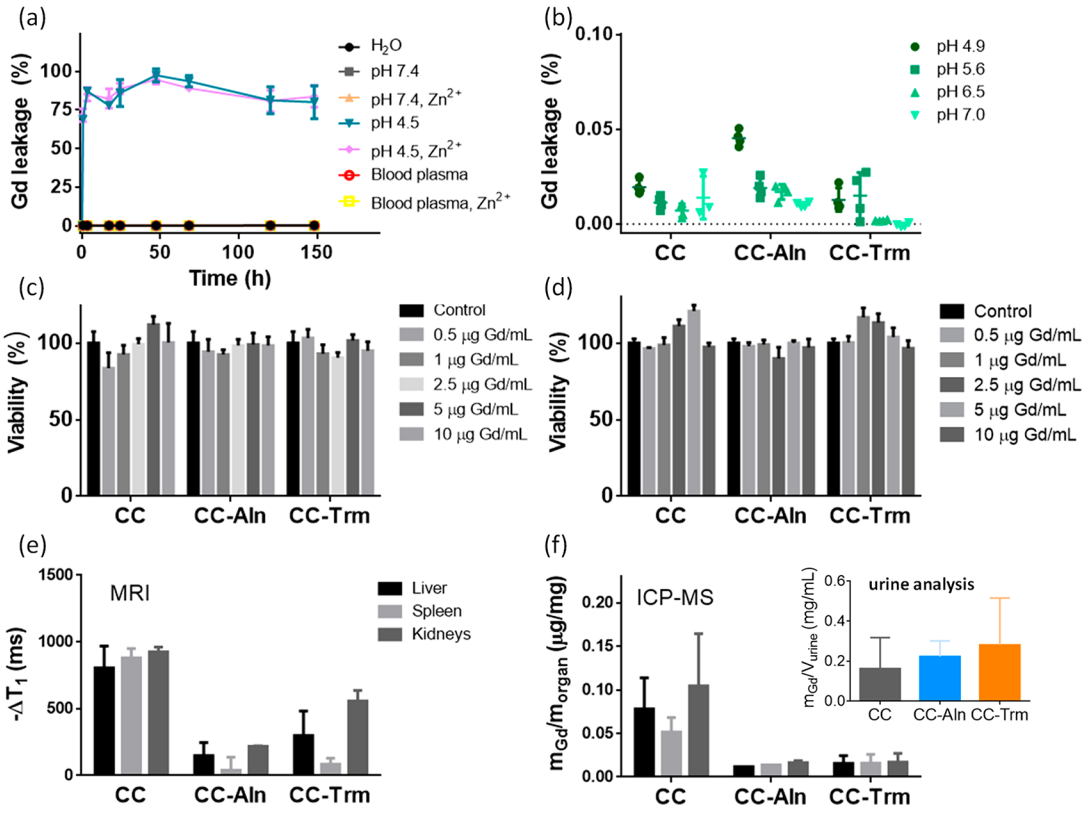

Figure 3. Biosafety and biodistribution. (a) Investigation of the Gd leakage from CC-NPs in different media with and without 2.5 mM Zn^{2+}. (b) Stability of Gd (III) entrapped within CC, CC-Aln, and CC-Trm NPs at different acidic pH values. (c) Cell viability of HepG2 treated with the three NPs at different concentrations (n = 3). (d) Cell viability of EA.hy926 treated with the three NPs at different concentrations (n = 3). (e) Decrease of positive MRI contrast in the organs where NPs accumulated after 1 h of the NP *i.v.* administration. (f) Quantitative analysis of Gd mass in liver, spleen, kidneys, and urine per weight of dried tissue (black, light gray, and dark gray bars correspond to liver, spleen, and kidneys) after MRI analysis (~2 h after NP *i.v.* administration).

dehydration of the amorphous CC core. This value was similar to reported data of amorphous CC NPs. The main release step of all samples is at 450 °C corresponding to the decomposition process of PAA as it indicated the weight loss derivative analysis of PAA and the three nanoprobes (Figure S12). The decomposition of the ligands Aln and Trm can be related to the smooth steps at 259 and 286 °C, respectively.

High Magnetic Relaxivity of Targeted MRI Nanoprobes. Gd-doped amorphous CC NPs have an unusually high longitudinal relaxivity (r_1)[22,23] that exceeds that of most commercial Gd-based contrast agents and even ultrasmall iron oxide-based NPs.[6,34,35] This is due to the high hydration and confinement of the gadolinium cations within the amorphous CC environment. However, the influence of surface chemical modifications of CC NPs on their magnetic relaxivity must be studied since previous reports with other types of nanoparticles have shown that these modifications can trigger the decay of the MR contrast.[36] To this end, we measured the longitudinal (T_1) and transversal (T_2) relaxation times of CC NPs at different concentrations for CC, CC-Aln, and CC-Trm NPs at 1.5 and 7 T in a minispec and in an MRI scanner, respectively (Figure 2a-b). Figure 2c summarizes the obtained data of relaxivity r_1 and the ratio between transversal and longitudinal relaxivity (r_2/r_1). They are compared with the commercial contrast agent Magnevist (Gd-DTPA, r_1= 4.1 mM^{-1} s^{-1}).[34] We found that all three nanoprobes were efficient T_1 contrast agents due to their high r_1 and low r_2/r_1 values. However, the r_1 of Aln and Trm functionalized CC NPs decreased by 27−68% compared to bared CC, likely due to modifications in the Gd^{3+} environment, such as the decrease in hydration observed in TGA measurements. Nevertheless, the r_1 of Aln and Trm functionalized CC NPs was still greater than 30 mM^{-1} s^{-1} at 1.5 T, outperforming synthetic or commercial contrast agents such as Magnevist (4.1 mM^{-1} s^{-1} at 1.5 T), and making them superior contrast agents for MRI.[35]

We evaluated the potential of our nanoprobes for *in vivo* studies by assessing the temporal stability of their MR contrast in blood plasma (Figure 2d). We measured the ratio r_2/r_1 of CC-Aln and CC-Trm for several days after preparation (day 0). The results showed a slight increase of r_2/r_1, possibly due to the formation of the protein corona as previously reported in the literature.[37,38] However, this increase remained almost constant for 1 week, and only a slight 1.2-fold and 1.1-fold increase was observed for CC-Aln and CC-Trim, respectively. This suggests that the positive MR contrast was not affected by the protein corona formation and no substantial colloidal aggregation had occurred. Unlike other positive MR contrast agents, our nanoprobes did not experience a significant increase in the r_2/r_1 ratio ($\Delta r_2/r_1 > 20$ times) due to the lack of colloidal stability.[38]

Biosafety and Biodistribution. Gd-based contrast agents are widely used contrast agents in medical imaging, but free Gd^{3+} can be toxic if not properly chelated or if it accumulates in the body over the long-term.[39] To ensure the biosafety of the nanoprobes, the stability of the Gd within the NPs was studied as well as cell viability and biodistribution. The possible leakage of Gd from the nanoprobes was studied at 37 °C and different time

https://doi.org/10.1021/acsnano.3c03523
ACS Nano 2023, 17, 13811−13825

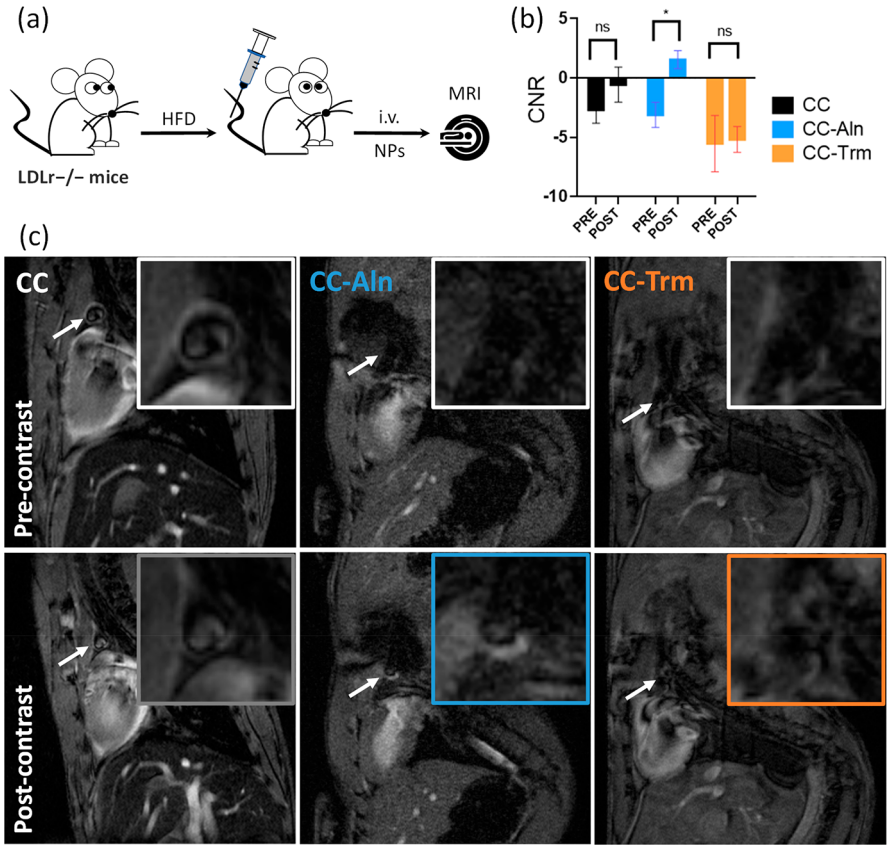

Figure 4. Targeted imaging of atherosclerosis with NPs *in vivo*. (a) Schematic of targeted MRI of atherosclerosis in LDLr−/− mice (4 months old) with amorphous CC NPs functionalized with different ligands (Aln and Trm). (b) Comparison of CNR enhancement of the aortic arch tissue with targeted CC NPs (CC vs CC-Aln and CC-Trm NPs). (c) T_1-weighted MRI before (precontrast) and after 1 h (postcontrast) of the i.v. administration of bare CC (gray), CC-Aln (blue), and CC-Trm (orange) NPs. The arrows indicate the position of the aorta, and the insets are magnified images of the aorta. Multiple *t* test statistical analysis. *$P < 0.05$, n.s. not significant *$P > 0.05$.

points for several days in various chemical and biological fluids, including water, phosphate buffer solution (PBS) at pH 7.4, citrate buffer at pH 4.5, and blood plasma (Figure 3a, Figure S12c). The Gd^{3+} released was measured by filtration (3 kDa molecular weight cutoff). Furthermore, the study investigated the ion exchange with Zn^{2+} in the same media. Zn is an essential metal for maintaining cellular homeostasis and is abundant in cells.[40,41] Therefore, transmetalation between Gd^{3+} and Zn^{2+} could be harmful in two ways, due to Gd^{3+} toxicity and a modification of Zn's buffering capacity, which could harm cells.[42] We found that at pH 4.5, CC NPs quickly lost their Gd content, likely due to calcium carbonate dissolution.[18] We then investigated the effect of pH on Gd leakage in the CC, CC-Aln, and CC-Trm samples in the pH range of 5−7. The results showed that all three NPs were highly stable, with measured Gd leakage of less than 0.05% at pH values as low as 4.9, as displayed in Figure 3b. This suggests that these NPs could remain stable in most biological environments, including atherosclerotic lesions where the pH ranges from 6.5 to 8.5.[43] Previous research by Dong et al. has shown that the presence of additives, such as poly(acrylic acid), enhances the stability of amorphous calcium carbonate nanoparticles.[23] Our study provides further evidence that the surface of these nanoparticles can be functionalized without compromising the Gd^{3+} content and the amorphous structure (Figure 1d,e). We also evaluated the cytotoxicity of these NPs using red blood cells, HepG2 hepatic cells, and EA.hy926 vascular endothelial cells after incubation with the three types of nanoprobes. These cell lines were chosen because the MR nanoprobes are designed for intravenous (i.v.) administration and thus are exposed to the lumen of the vascular wall before accumulating in typical clearance organs, such as the liver or the spleen. The results showed no necrotic effects or obvious cytotoxicity at the highest concentration (10 μg Gd/mL, 1 mg NP/mL) after 3 and 24 h (Figure S13, Figure 3c, d and Figure S14a,b), or even after 48 h (Figure S14c,d), indicating low cytotoxicity *in vitro*.

Finally, the organ biodistribution of the three nanoprobes was investigated in a healthy murine model (C57BL/6 mice), after i.v. administration using MRI. The three NPs (at a dose of 0.1 mmol of Gd/kg of mouse) were found to accumulate the most in the liver, spleen, and kidneys, as seen in Figure 3e. Notably, the kidneys showed high accumulation of all three NPs, indicating partial renal clearance that is beneficial in preventing long-term NP accumulation in the body. ICP-MS analysis of both the organs and urine confirmed this finding (Figure 3f). The higher values of ΔT_1 for CC NPs, as observed in these experiments conducted at a constant dose of Gd, are justifiable given their higher r_1 values (Figure 2). However, the higher Gd accumulation in organs observed in Figure 3f could imply that CC NPs clear from the bloodstream faster than CC-Aln and CC-Trm NPs. While the presence of Gd in urine indicates its existence, the heterogeneity of this measurement makes a quantitative comparison impossible. Lastly, the study confirmed that the accumulation of the three nanoprobes in the aortic wall was insignificant in the absence of atherosclerotic plaques, as depicted in Figure S15.

https://doi.org/10.1021/acsnano.3c03523
ACS Nano 2023, 17, 13811−13825

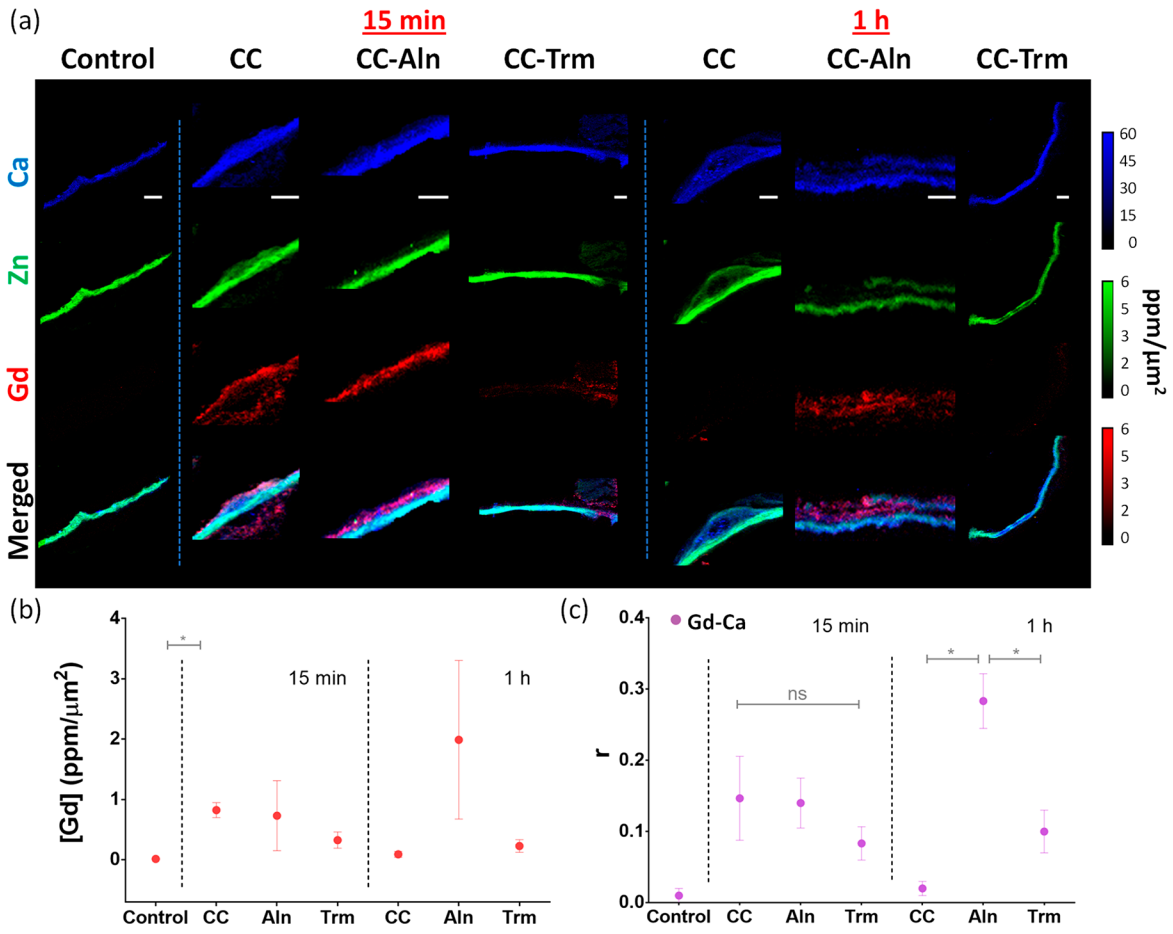

Figure 5. SXRF imaging of NPs in atherosclerotic aortas *ex vivo*. (a) Representative SXRF Ca, Zn and Gd elemental and composite maps of 50 μm thick longitudinal sections of aortas from LDLr−/− mice model of atherosclerosis untreated or treated with a single i.v. administration of Gd-doped CC, CC-Trm or CC-Aln NPs (0.05 mmol/kg) for 15 or 60 min, obtained using incident energy 11 keV at 5 × 5 μm^2 step size; scale bar 500 μm. Images were generated in FIJI ImageJ package.[56] (b) Comparison of average Gd accumulation/area unit (as ppm Gd/μm^2) in the aortic tissue analyzed with SXRF in (a). (c) Ca−Gd correlation (shown as r-Pearson correlation coefficient) in the aortic tissue analyzed with SXRF in (a). Multiple *t* test statistical analysis. *P < 0.05, n.s. not significant *P > 0.05.

Comparative Study of Ligand-Mediated Targeting in Atherosclerosis. After verifying the stability and biosafety of our MR nanoprobes, we proceeded to examine the targeting and MR imaging capabilities of CC-Aln and CC-Trim NPs toward calcifications and macrophages *in vivo*, which are both crucial hallmarks of atherosclerosis.

Calcifications, which range in size from a few to hundreds of micrometers, are a clinical marker of atherosclerosis. The amount, shape, and position of the calcifications within the plaque play critical roles in plaque homeostasis. Microcalcifications and spotty calcifications may be involved in an active stage of plaque progression and in the plaque rupture due to the loss of elasticity of the artery, whereas calcifications neighboring the aortic adventitia can be found in stable plaques.[44] Consequently, the medical imaging and characterization of calcifications thanks to specific contrast agents could be a vital diagnostic tool.[16] Previous studies have demonstrated that Ca-targeted NPs originally designed for bone applications, can be successfully repurposed to image vascular calcifications, given the similarities of both biomaterials (both made of HAP).[45] These NPs were functionalized with Ca-targeting peptides and bisphosphonate ligands. Bisphosphonates' affinity for HAP stems from their chemical resemblance to pyrophosphates, which regulate HAP formation in the body. We chose alendronate for CC functionalization because it is a bisphosphonate ligand that has recently been applied in imaging microcalcifications.[16]

Monocyte-derived macrophages play a critical role in the pathogenesis and progression of atherosclerosis.[46] However, as macrophages are a heterogeneous population of cells, different subtypes could exhibit either pro-or antiatherosclerotic properties. Therefore, nanoprobes must be capable of specifically targeting the expression of different biomarkers characteristic of pro-atherosclerotic macrophages to provide valuable insights into both atherosclerosis progression and quantification of atherosclerosis burden.[25] In this context, macrophages with increased expression of mannose receptors have been described as pro-atherosclerotic.[26] Thus, the effective targeting of macrophages by specific binding to mannose receptors may offer a promising approach for imaging atherosclerotic plaques. To this end, we modified the surface of CC NPs with customized mannose ligands (amino-terminated branched trimannose), which are known to improve the macrophage uptake of NPs.[45]

In vivo MR imaging studies were conducted using a mouse model deficient in low-density lipoprotein receptor deficiency (LDLr−/−) (Figure 4a). This model was selected because it is one of the most commonly used for studying fundamental biological aspects of atherosclerosis, new treatments, and

https://doi.org/10.1021/acsnano.3c03523
ACS Nano 2023, 17, 13811−13825

diagnostic tools.[47,48] CC-Aln, CC-Trm and bare CC NPs were administered i.v. at a dose of 0.1 mmol Gd/kg, and images of the three groups of animals (n= 3) were obtained after 1 h. We then analyzed the contrast-to-noise-ratio (CNR) of the aortic arch tissue before and after the administration of the three types of NPs (Figure 4b,c). CNR values provide quantitative information on signal-to-noise ratio (SNR) enhancement and targeted imaging efficacy, taking into account the background signal. CNR enhancement with contrast agents increases the perception of distinct differences between tissues and biological events, such as inflammation. Moreover, it is a value that can be compared across MRI scanners of varying magnetic fields.[49] In our experiments, the CNR was defined as the difference between the SNR of the aortic arch tissue and the SNR of the muscle tissue ($CNR = SNR_{AA}\text{-}SNR_{M}$). Figure 4b demonstrates that the CNR increased after the administration of all three nanoprobes, but only CC-Aln NPs provided the greatest and significantly different CNR enhancement due to ligand targeting. In contrast, the ligand Trm resulted in negligible accumulation of CC-Trm after 1 h. Figure 4c shows representative MRI images of the targeted imaging of CC-Aln NPs in the aortic arch tissue, which were also observed in other segments of the aorta, specifically in the sections near the kidneys (Figure S16). The results also show some accumulation of bare NPs, but considering their higher r_1 value and similar NP dose, it can be assumed that the concentration of NPs in the tissue was much lower than that of CC-Aln. The efficacy of CC-Aln NPs in imaging atherosclerotic plaques was further demonstrated using Apoe−/− mice, another well-established mouse model of atherosclerosis, as shown in Figure S17. Our study employed MRI to image the significant difference in NP accumulation resulting from ligand-mediated targeting. Comparative studies on ligand-mediated atherosclerosis imaging with NPs are scarce to our knowledge. Kim et al. demonstrated an increased accumulation of iron oxide-based contrast agents targeting the plaque neovasculature compared with similar NPs targeting the fibrous cap,[15] but these results were obtained *ex vivo* by analyzing the aortic tissue after NP administration by fluorescence and MRI. One of the challenges in imaging atherosclerosis is standardizing contrast agents to allow comparative studies between different biological targets using noninvasive methods such as *in vivo* MRI.[10] Our results indicate that Gd-doped CC NPs are a valuable tool in this field due to the MRI contrast enhancement and the insignificant accumulation of bare CC NPs within the plaques, whose permeability is enhanced compared to healthy aortic tissue.[50] To understand the lower ligand-mediated targeting of CC-Trm compared to CC-Alen NPs, we analyzed the aorta tissues using two distinct methods: histology and synchrotron X-ray Fluorescence (SXRF) analysis.

***Ex Vivo* Evaluation of Ligand-Mediated Targeted Imaging of Atherosclerosis.** Aortas from LDLr−/− mice treated with saline solution or the various CC NPs (CC, CC-Trm, or CC-Aln; 0.05 mmol NPs/kg) were extracted and preserved in paraffin or cryopreserved in an optimal cutting temperature (OCT) compound. Cross sections of both 4 and 50 μm thickness were generated and deposited on either glass slides for histology or sapphire discs for *ex vivo* analysis using synchrotron X-ray fluorescence (SXRF) analysis. Histological analysis of the aortas from our LDLr−/− atherosclerotic mouse model confirmed the presence of early stage atheromas with a few microcalcifications that were revealed through Alizarin Red staining. A reduced presence of macrophages (due to their infiltration into the arterial wall) was confirmed through an anticluster of differentiation 68 (CD68) immunohistochemistry analysis. Data are presented in Figure S18.

SXRF maps and spectra (Figure 5, Figures S19−S26) were acquired at room temperature using a beamline I18 (Diamond Light Source UK), with an energy set at 11 keV and focused at 5 × 5 μm^2 to analyze aorta areas selected by brightfield microscopy. SXRF is a quantitative analytical method that uses X-rays to excite electrons at the inner orbitals of atoms and obtain distinctive emission signals from each element. When combined with scanning acquisition strategies, it allows for generating maps that show the spatial distribution of different chemical elements within the same sample section.[51,52] This technique was ideal for providing quantitative information about the ability of the different Gd-doped CC NPs (CC, CC-Trm, or CC-Aln) to accumulate within atherosclerotic arteries. We included a second time point (15 min) to explore the temporal dimension in the accumulation of CC NPs (with and without targeting ligand) in the plaque and compared it with not-injected mice. The time points of 15 min and 1 h were selected based on preliminary results and previous research.[23] At 15 min, CC NPs were still circulating in the blood, while after 1 h, significant accumulation occurred in organs (liver, spleen, kidneys) as shown in Figure 3e,f. As expected, aortas from these untreated animals used as controls did not show Gd-related SXRF emission (Figure 5a, Figure S19). In contrast, Gd-L fluorescence peaks of different intensities were visible in aorta sections of mice treated with the various CC NPs (Figure S19). Initial analysis of the SXRF maps showed that all CC NPs mainly accumulated at the surface of areas with high concentrations of Zn (Figure 5a, Figures S20−S26). These Zn-rich areas are normally associated with cellular tissue, as this metal is highly concentrated in the nuclei of cells.[53,54] Thus, it seems likely that the NPs accumulate in areas around the endothelium of the aortic tissue, as expected when targeting atherosclerotic plaque. Bare CC NPs and CC-Trm NPs targeting inflammation (CC-Trm NPs) were observed at short experimental times (average accumulations of 0.82 ± 0.12 and 0.33 ± 0.13 ppm Gd/μm^2 respectively after 15 min postinjection), but CC-NPs were removed from the arteries promptly, while CC-Trm NPs slightly decrease their concentration (average accumulations of 0.09 ± 0.05 and 0.23 ± 0.10 ppm Gd/μm^2 respectively after 60 min). On the other hand, CC-Aln NPs, which were designed to target calcifications, showed a gradual and significant time-dependent accumulation (averaging 0.73 ± 0.58 ppm Gd/μm^2 after 15 min and 1.99 ± 1.31 ppm Gd/μm^2 with multiple areas showing more than 10 ppm Gd/μm^2 after 60 min treatment). These *ex vivo* results obtained through SXRF analysis were consistent with the *in vivo* MRI findings, confirming that CC-Aln NPs are more efficient and specific in targeting atherosclerotic plaques compared to the other CC NPs tested (Figure 5a-b, Figures S20−S26).

The selective accumulation and persistence of CC-Aln NPs in the aorta of atherosclerotic mice after i.v. administration suggest that alendronate targeting guides CC NPs to the lipid-rich core of the atherosclerotic plaque, which other NPs fail to reach and are eliminated. This may explain the enhanced correlation between Ca and Gd at longer experimental times in mice treated with CC-Aln, and the decrease in those treated with bare CC or CC-Trm NPs (Figure 5c). Further studies involving different arterial calcification scores and atherosclerosis progression stages are necessary to better comprehend the colocalization of Gd-doped CC-Aln and calcifications. Nonetheless, the

https://doi.org/10.1021/acsnano.3c03523
ACS Nano 2023, 17, 13811−13825

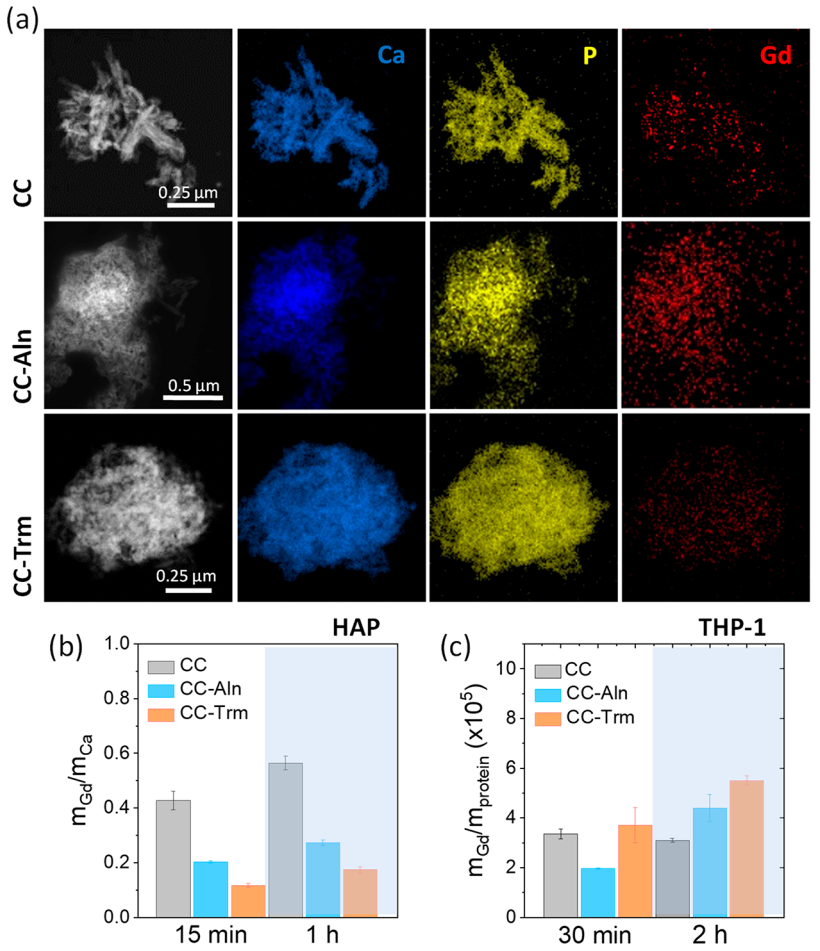

Figure 6. Targeting *in vitro*. EDX analysis of adsorption of CC-Aln for HAP compared to CC-Trm. STEM images of HAP and corresponding element mapping of HAP components (Ca and P) and Gd present in CC-Aln and CC-Trm (a). ICP-MS measurements of Gd adsorbed on the HAP samples after 5 and 15 min of incubation (b). NP uptake studies with THP-1 derived macrophages determining the amount of Gd by ICP-MS per cellular protein.

presence of early stage atheroma plaque in the histological analysis (Figure S18), the MRI results (Figure 4) and the SXRF analysis suggests that CC-Aln NPs could serve as useful contrast agents for early detection of atherosclerosis. Interestingly, the limited number of macrophages observed in the histological analysis of atheromas (Figure S18) correlates with the low accumulation of CC-Trm NPs seen in MRI and SXRF. However, to gain further insight into the specificity of the interactions between the various CC NPs and their corresponding targets, HAP, and macrophages, we studied these interactions *in vitro*.

In Vitro Evaluation of Ligand-Mediated Targeting. To investigate the observed differences in the aortic accumulation of the various CC NPs *in vivo* and *ex vivo*, additional experiments were performed to evaluate ligand-mediated targeting *in vitro*. First, the specificity of the adsorption of CC, CC-Aln, and CC-Trm to HAP microparticles (the main component of calcifications) was compared at physiological pH and different incubation times (15 min and 1 h). The amount of each type of CC NPs that remained adsorbed on the HAP microparticles was determined after the incubation of both particles and several washing steps. Energy-dispersive X-ray spectroscopy (EDX) and ICP-MS were used to confirm the colocalization of Gd on the HAP microparticle surface, which main characteristic atomic components are Ca and P, (Figure 6a, Figure S27) and calculate the ratio of [Gd]/[Ca] (Figure 6b, Figure S28), respectively. The results indicated a higher presence of CC-NPs on the HAP microparticles compared to CC-Aln and CC-Trm NPs, possibly due to a faster and nonspecific attractive interaction between CC-NPs and HAP, which has also been observed *ex vivo* by SXRF at 15 min postadministration (Figure 5). The CC NPs may be adsorbed on HAP surface microparticles through electrostatic interactions or hydrogen bonds between the carboxylic groups of the PAA in CC NPs and the surface groups of HAP at physiological pH. Previous studies have shown that PAA (partially exposed on the CC NP surface) can adsorb on HAP and bone samples.[56] However, bisphosphonates are the most widely used drugs for diseases involving bone resorption. Among these drugs, alendronate has one of the highest binding affinities to HAP and lowest reversible adsorption,[57,58] which may explain why CC-Aln NPs were not washed out of the atherosclerotic plaque over time *in vivo*, leading to an increase of their concentration in the aortic tissue and enhanced the MR signal of aortas. Additionally, we evaluated the ability of CC-Trm to target monocyte-derived macrophages *in vitro* and found an increase in their uptake compared with their counterparts, CC and CC-Aln NPs at two different time points (30 min and 2 h), as displayed in Figure 6c. This could support the idea that the reduced accumulation of these NPs in *vivo* is due to the reduced presence of macrophages expressing the mannose receptor.

https://doi.org/10.1021/acsnano.3c03523
ACS Nano 2023, 17, 13811−13825

However, as suggested above, further studies with atheroma plaques at different stages of inflammation will be necessary to validate the application of these nanoprobes.

3. CONCLUSIONS

In the field of atherosclerosis imaging, the development of nanoparticles that can be detected noninvasively, such as through MRI, could have significant clinical benefits for diagnosis (plaque detection and risk assessment) and therapy. To this aim, it is necessary to develop nanoplatforms that allow for easy surface modification with different ligands, targeting the main hallmarks of atherosclerotic lesions *in vivo*, and the implementation of advanced analytical techniques that aid in understanding the interactions between these nanoplatforms and the plaque. In this context, we demonstrated that Gd (III)-doped amorphous calcium carbonate nanoparticles are an excellent nanotool for screening different targeted ligands due to their high MRI contrast and their physicochemical properties that provide high Gd stability, easy surface functionalization, and partial renal clearance.

In this study, we successfully conjugated alendronate and trimannose ligands to amorphous calcium carbonate nanoparticles to target plaque calcifications and macrophages, respectively. We characterized the MRI nanoprobes, confirming the stability of Gd (III) and the maintenance of the amorphous structure of the nanoparticles after chemical modification as well as the *in vitro* targeting ability of ligand-functionalized nanoparticles. Using MRI and synchrotron XRF tissue analysis, we demonstrated that alendronate-functionalized nanoparticles provided specificity for atheroma imaging, whereas bare nanoparticles were initially accumulated in the plaque but washed out over time. The results with the trimannose ligand showed less efficient accumulation likely due to the early stage of the atheroma plaque progression.

The conclusions of our study indicate that a high binding affinity between the ligand and targeted tissue is essential to overcome the clearance of nanoparticles that are adsorbed at the endothelium of the aorta. The affinity of the alendronate ligand for calcifications allowed for nanoparticle accumulation over time in the atherosclerotic plaque, leading to a significant increase in contrast-to-noise ratio signal in MRI. Our study used a combination of noninvasive MRI, *in vitro* targeting studies, and advanced *ex vivo* analysis by XRF, highlighting the importance of interdisciplinary studies to decipher the interaction between nanoparticles and biological systems for effective targeted imaging of atherosclerotic lesions and future early diagnosis and plaque vulnerability assessment.

Experimental Section. *Materials.* Anhydrous sodium carbonate ≥99.0 (Na_2CO_3) was purchased from Fluka. Anhydrous calcium chloride 97% ($CaCl_2$) was purchased from Riedel-de Haën. Poly(acrylic acid sodium salt) average M_w ~2100, gadolinium(III) chloride hexahydrate ($GdCl_3{\cdot}6H_2O$), 1-ethyl-3-(3-dimethylaminopropyl) carbodiimide (EDC), N-hydroxysulfosuccinimide sodium salt (sulfoNHS), hydroxyapatite (HAP) and alendronate (Aln) sodium trihydrate were purchased from Sigma-Aldrich. The customized synthesis of the amino-terminated trimannose ligand is described in detail in the Supporting Information (SI). All solutions were prepared using nanopure water as the solvent (Thermo Scientific Barnstead Nanopure).

Synthesis of Amorphous Calcium Carbonate Nanoparticles Doped with Gadolinium. CC NPs were prepared according to previous reports with slight modifications, mainly in the purification process.[23] Briefly, 686.4 mg of $CaCl_2$ and 7.68 g of poly(acrylic acid) (PAA, M_w~2100) were dissolved and mixed in 60 mL of nanopure H_2O water and then mixed with 316.32 mg of $GdCl_3{\cdot}6H_2O$, under vigorous stirring at room temperature. Finally, 60 mL of $NaCO_3$ (10.6 mg/mL) was added and stirred for one minute. To terminate the reaction, 120 mL of ethanol was added. This mixture was centrifuged for 2 min at 3000 rpm once, and then, the precipitate was resuspended in 10 mL of nanopure H_2O and washed by ultrafiltration with 3 kDa AMICON. All samples were lyophilized and stored at room temperature.

Surface Functionalization of CC NPs. Lyophilized CCs (25 mg) were resuspended in water and added to a vial with 26.6 mg of EDC and 32.6 mg of sulfo-N-hidroxisulfosucinimida (sulfo-NHS). This mixture was stirred for 30 min to activate the carboxylic groups. After that, ultracentrifugation was performed with 3 kDa molecular weight cutoff AMICON filters (0.5 mL each filter) at 12500 rpm, 20 min. The retentate was then resuspended in 0.01 M PBS (pH 8). This suspension was added to a vial with 1 mg of the desired ligand (alendronate or trimannose) and left to incubate for 1 h at room temperature. Finally, the functionalized CCs were purified by ultracentrifugation using 3 kDa AMICON filters to eliminate unreacted species.

Characterization. AFM imaging was performed on mica substrates by using a Veeco Multimodel AFM attached to a Nanoscope V controller. The samples were imaged in tapping mode in air, using a V-TESPA probe with k = 42 N/m. ICP-MS measurements were performed on a Thermo iCAP Q ICP-MS (Thermo Fisher Scientific GmbH, Bremen, Germany), coupled to an ASX-560 autosampler (CETAC Tech, Omaha, NE, USA). Dynamic Light Scattering (DLS) was used to measure the hydrodynamic diameter and zeta potential of CCs using a Malvern Zetasizer Nano-ZS instrument (Malvern Instrument, Malvern, UK). Thermogravimetric analyses were performed under air (25 mL·min^{-1} flow rate) using a TGA Discovery (TA Instruments). The samples were equilibrated at 100 °C for 20 min to eliminate humidity and then heated at a rate of 10 °C·min^{-1} from 100 to 800 °C. X-ray photoelectron spectroscopy (XPS) experiments were performed in a SPECS Sage HR 100 spectrometer with a nonmonochromatic X-ray source (aluminum Kα line of 1486.7 eV energy and 252 W), placed perpendicular to the analyzer axis and calibrated using the $3d_{5/2}$ line of Ag with a full width at half-maximum (fwhm) of 1.1 eV.

Magnetic Relaxometry. The Magnetic relaxivities of the nanoprobes were measured in a Bruker Minispec MQ60 (Bruker Biospin GmbH) contrast agent analyzer at 1.5 T at 37 °C. Additionally, T_1 and T_2 were also measured in a 7 T horizontal bore Bruker Biospec USR 70/30 MRI system (Bruker Biospin GmbH). The relaxivities r_1 and r_2 were obtained by plotting 1/T against the gadolinium concentration (mM) measured by ICP-MS.

Nanoparticle Stability Assays. Gd leakage and transmetalation were studied by incubating 1 mg of CC NPs in 0.5 mL of the corresponding buffer (H_2O, PBS pH 7.4, PBS pH 7.4 + Zn^{2+}, citrate buffer pH 4.5 and citrate buffer pH 4.5+ Zn^{2+}), blood plasma, blood plasma + Zn^{2+}, at 37 °C for different time points. At each time point, samples were filtrated with 3 kDa AMICON filters at 13000 rpm for 10 min. The filtrates were analyzed by ICP-MS to determine the Gd leakage. The hydrodynamic diameter of the nanoprobes and the magnetic

https://doi.org/10.1021/acsnano.3c03523
ACS Nano 2023, 17, 13811−13825

relaxivities were also measured for several days after the synthesis to verify their colloidal and magnetic stability.

Cytotoxicity Analysis. First, we analyzed the impact of CC, CC-Aln and CC-Trm NPs on cellular mitochondrial activity using 3-(4,5-dimethylthiazol-2-yl)-2,5-diphenyl tetrazolium bromide (MTT) assay in two cell cultures, EA.hy926 vascular endothelial cells and HepG2 hepatic cells, at three different times (24, 48, and 72 h) and five different NP concentrations (results included in the Supporting Information). Next, we studied whether the observed low cytotoxicity was due to apoptosis or necrosis with the Annexin V Apoptosis Detection Kit APC (Ebioscience #88-8007-72). Briefly, EA.hy926 cells (25.000 cells/well) were seeded in 24-well plates 1 day prior to NP incubation. The three types of NPs were administered to cells at different concentrations, and after 24 h of incubation, the cells were washed twice with DPBS. Cells were then harvested with trypsin/EDTA and stained with the Annexin V kit following the product instructions. Cells were incubated for 15 min with 5 μL of Annexin V diluted with 200 μL of binding buffer. After 15 min, cells were washed with binding buffer, and 5 μL of propidium iodide was added prior to flow cytometry analysis. Results were obtained with BD FACSCanto II and analyzed by Flow Jo v7 software.

Biodistribution Analysis. C57BL6 male mice were i.v. with a dose of 0.1 mmol of Gd/kg mouse. The biodistribution study was performed after 1 h of NP i.v. administration in the tail vein. The experiments were carried out on a 7 T Bruker Biospec 70/30 USR MRI system (Bruker Biospin GmbH, Ettlingen, Germany) interfaced to an AVANCE III console. A BGA12 imaging gradient system (maximum gradient strength 400 mT/m) with a 40 mm diameter quadrature volume resonator was employed for MRI data acquisition. The quantification was performed with T_1-weighted maps, which were obtained using a spin echo saturation recovery with a variable repetition time Bruker RAREVTR method. T_1 maps were obtained before and after administration at eight different T_R values (9000, 5000, 3000, 2000, 1500, 1000, 600, and 427 ms) with an effective T_E of 16 ms, RARE factor 4, four averages, 110 × 110 points, a field of view of 3.2 cm × 3.2 cm, and 10 slices with a slice thickness of 1.0 mm and a 1.0 mm gap between slices. The T1 maps were created with a customized python-based script and reconstructed to a matrix of 128 × 128. The final T_1 map values were measured by defining different regions of interest (ROIs) for each organ by using ITK-SNAP software.

Targeted MRI of Atherosclerosis with Functionalized CC Nanoparticles. NP targeting experiments were performed with four-month-old LDLr−/− male mice fed a high-fat diet for 4−6 weeks to induce atherosclerosis. For imaging and NP administration, the animals were first anesthetized with a mixture of 3−5% isofluorane and then maintained at 1.5−2% in 50% O_2. Our nanoprobes were injected into the tail vein at a dose of 0.1 mmol Gd/kg (100 μL) and one h later, 7 T MRI images were acquired in the aortic arch and abdominal regions near the renal bifurcation. To ensure accurate and reproducible positioning, pure axial and four-chamber view scout images were used to set up the representative aortic arch view. Images were obtained between the brachiocephalic artery and left common carotid artery, perpendicular to the direction of the flow in the aorta. A single 0.8 mm, 2.8 × 2.8 cm isotropic FOV (obtained and reconstructed with 256 × 256) slice was obtained using a Bruker self-gated cine gradient echo FLASH sequence using the following parameters: minimum T_E of 4 ms, T_R of 9 ms, and flip angle of 10°, on average. Additional images in the same animal bed position were obtained with a fat suppression module. Aortic renal bifurcation images were acquired with a relaxation enhancement (RARE; fast/turbo spin echo) sequence. Twenty slices of 0.8 mm, isotropic FOV 32 × 32 mm (obtained and reconstructed with 256 × 256) were acquired using the following parameters: T_E = 14 ms, T_R = 1200 ms, RARE factor = 4, and three averages. All animal bioimaging experiments were performed in accordance with the Spanish policy for animal protection (RD53/2013), which meets the requirements of the European Union directive 2010/63/UE, at CIC biomaGUNE animal facility. The procedures were approved by the Ethical Committee of CIC biomaGUNE and authorized by the local authorities (Diputación Foral de Guipúzcoa, PRO-AE-SS-120).

SXRF Analysis. Atherosclerotic mice were treated with a single intravenous injection of Gd-doped CC NPs (0.05 mmol/kg), either unlabeled or labeled with different peptides targeting microcalcification (Alendronate) or inflammation (Trimanose). Saline serum-injected mice were used as controls. After 15 or 60 min, the animals were perfused with 4% paraformaldehyde in a 0.9% saline solution with heparin (10 U/ml). Their aortas were isolated, cryoprotected using 20% sucrose, embedded in cryomoldeds using OCT, and stored at −80 °C until sectioned. Then 50 μm-thick cross sections were generated and deposited on sapphire discs and visualized using a brightfield microscope to select areas of the aortas for SXRF analysis at the I18 beamline at the Diamond Synchrotron Light Source (Oxford, UK). Both sections of the arch and the renal part of the aortas were obtained.

Irradiation of the samples was carried out using a beam focused at 5 × 5 μm^2, and energy fixed to 11 keV (flux between 1.6 and 2.5 × 10^{11} ph/s). Detection was performed using two 4-element Vortex silicon drift detectors (Hitachi). Scan step size was fixed at 50 × 50 μm^2 (dwell time 50 ms) for coarse scans to optimize the measurement parameters. Following this, at least three high-resolution SXRF elemental maps were collected for each sample using 5 × 5 μm^2 scan steps (dwell times 50 ms or 0.5 s). The raw maps were processed using the free PyMCA software.[59] Concentration maps were produced assuming a matrix of 50 μm-thick soft tissue, while the quantitative calibration was determined using a thin film X-ray fluorescence 7-element reference sample (AXO Dresden GmbH). The concentration maps were further processed using FIJI ImageJ package.[55]

In Vitro Targeting Assays. The interaction between HAP and our nanoprobes was studied with EDX and ICP-MS. Commercial HAP (200 μL, 1.2 mg/mL) was mixed under stirring with 20 μL of CC-Aln or CC-Trm solutions at [Gd] = 9 mM for 5 and 15 min at 37 °C. After that, the samples were precipitated and washed twice by centrifugation to remove the unattached NPs (10.000 rpm, 10 min). Then, the ratio [Gd]/[Ca] of HAP after the incubation and washing steps was measured by EDX and ICP-MS for the two types of NPs. Next, we studied the NP cell uptake with THP-1 derived macrophages. Briefly, human monocytes THP-1 cells were grown in suspension in RPMI with 10% (v/v) fetal bovine serum (FBS), 0.05 mM of β-mercaptoethanol (Sigma-Aldrich) and 1% (v:v) antibiotic solution (100 units/mL penicillin, 100 mg/mL streptomycin, P/S) in a humidified 37 °C and 5% CO_2 incubator. THP-1 cells were seeded at 180 000 cells/well in 24-well plates and differentiated to the M0 phenotype. They were incubated for 72 h with 150 nM phorbol 12-myristate 13-acetate (PMA) (Sigma-Aldrich), followed by 24 h of incubation with RPMI medium. Then, the macrophages were incubated for

https://doi.org/10.1021/acsnano.3c03523
ACS Nano 2023, 17, 13811−13825

30 min and 2 and 4 h with CC-Aln and CC-Trm NPs. After the incubation, the cells were washed twice with cold Dulbecco's phosphate buffered saline (DPBS), and 150 μL of cold RIPA buffer (abcam no. ab156034) with protease inhibitor (Fisher scientific no. 10320015) was added to each well to lyse the cells. After 30 min of incubation on ice, 50 μL was collected for protein determination with the BCA assay (Thermo Scientific 23227) following the product protocol. The rest of the solution (100 μL) was digested with 1 mL of 2% nitric acid for ICP-MS analysis. More details about this section can be found in the SI.

ASSOCIATED CONTENT

Supporting Information

The Supporting Information is available free of charge at https://pubs.acs.org/doi/10.1021/acsnano.3c03523.

> Synthesis of branched trimannoside ligand, chemical structure of alendronate ligand, physicochemical characterization of the different nanoprobes (UPLC, TEM, STEM, FT-IR, XPS and TGA), biosafety studies (including hemolysis assay and viability assays), additional MRI studies confirming ligand-mediated targeting, histological analysis, additional information about the SXRF analysis and quantitative EDX analysis (PDF)

AUTHOR INFORMATION

Corresponding Authors

Jesús Ruiz-Cabello − *Center for Cooperative Research in Biomaterials (CIC biomaGUNE), Basque Research and Technology Alliance (BRTA), 20014 Donostia, Spain; CIBER de Enfermedades Respiratorias (CIBERES), 28029 Madrid, Spain; Ikerbasque, Basque Foundation for Science, 48013 Bilbao, Spain; Departamento de Química en Ciencias Farmacéuticas, Universidad Complutense de Madrid, 28040 Madrid, Spain;* orcid.org/0000-0001-8681-5056; Email: jruizcabello@cicbiomagune.es

Susana Carregal-Romero − *Center for Cooperative Research in Biomaterials (CIC biomaGUNE), Basque Research and Technology Alliance (BRTA), 20014 Donostia, Spain; CIBER de Enfermedades Respiratorias (CIBERES), 28029 Madrid, Spain; Ikerbasque, Basque Foundation for Science, 48013 Bilbao, Spain;* orcid.org/0000-0003-1444-6268; Email: scarregal@cicbiomagune.es

Authors

Lydia Martínez-Parra − *Center for Cooperative Research in Biomaterials (CIC biomaGUNE), Basque Research and Technology Alliance (BRTA), 20014 Donostia, Spain; Euskal Herriko Unibertsitatea (UPV/EHU), 20018 Donostia, Spain*

Marina Piñol-Cancer − *Center for Cooperative Research in Biomaterials (CIC biomaGUNE), Basque Research and Technology Alliance (BRTA), 20014 Donostia, Spain; Euskal Herriko Unibertsitatea (UPV/EHU), 20018 Donostia, Spain; CIBER de Enfermedades Respiratorias (CIBERES), 28029 Madrid, Spain*

Carlos Sanchez-Cano − *Donostia International Physics Center, Donostia 20018, Spain; Ikerbasque, Basque Foundation for Science, 48013 Bilbao, Spain; Polimero eta Material Aurreratuak: Fisika, Kimika eta Teknologia, Kimika Fakultatea, Euskal Herriko Unibertsitatea (UPV/EHU), 20018 Donostia, Spain;* orcid.org/0000-0002-9522-0019

Ana B. Miguel-Coello − *Center for Cooperative Research in Biomaterials (CIC biomaGUNE), Basque Research and Technology Alliance (BRTA), 20014 Donostia, Spain*

Desirè Di Silvio − *Center for Cooperative Research in Biomaterials (CIC biomaGUNE), Basque Research and Technology Alliance (BRTA), 20014 Donostia, Spain*

Ana M. Gomez − *Instituto de Química Orgánica General, IQOG-CSIC, 28006 Madrid, Spain;* orcid.org/0000-0002-8703-3360

Clara Uriel − *Instituto de Química Orgánica General, IQOG-CSIC, 28006 Madrid, Spain*

Sandra Plaza-García − *Center for Cooperative Research in Biomaterials (CIC biomaGUNE), Basque Research and Technology Alliance (BRTA), 20014 Donostia, Spain*

Marta Gallego − *Center for Cooperative Research in Biomaterials (CIC biomaGUNE), Basque Research and Technology Alliance (BRTA), 20014 Donostia, Spain*

Raquel Pazos − *Center for Cooperative Research in Biomaterials (CIC biomaGUNE), Basque Research and Technology Alliance (BRTA), 20014 Donostia, Spain*

Hugo Groult − *Biotechnologies et Chimie des Bioressources pour la Santé, Littoral Environment et Sociétés (LIENSs Laboratory), UMR CNRS 7266, 17000 La Rochelle, France;* orcid.org/0000-0002-1571-9400

Marc Jeannin − *Laboratoire des Sciences de l'Ingénieur pour l'Environnement (LaSIE), UMR-CNRS 7536, La Rochelle Université, 7356 La Rochelle, France*

Kalotina Geraki − *Diamond Light Source, Didcot OX11 0DE, United Kingdom*

Laura Fernández-Méndez − *Center for Cooperative Research in Biomaterials (CIC biomaGUNE), Basque Research and Technology Alliance (BRTA), 20014 Donostia, Spain; Euskal Herriko Unibertsitatea (UPV/EHU), 20018 Donostia, Spain; CIBER de Enfermedades Respiratorias (CIBERES), 28029 Madrid, Spain*

Ainhize Urkola-Arsuaga − *Center for Cooperative Research in Biomaterials (CIC biomaGUNE), Basque Research and Technology Alliance (BRTA), 20014 Donostia, Spain*

María Jesús Sánchez-Guisado − *Center for Cooperative Research in Biomaterials (CIC biomaGUNE), Basque Research and Technology Alliance (BRTA), 20014 Donostia, Spain; Euskal Herriko Unibertsitatea (UPV/EHU), 20018 Donostia, Spain; CIBER de Enfermedades Respiratorias (CIBERES), 28029 Madrid, Spain*

Juliana Carrillo-Romero − *Center for Cooperative Research in Biomaterials (CIC biomaGUNE), Basque Research and Technology Alliance (BRTA), 20014 Donostia, Spain; Basque Res & Technol Alliance BRTA, GAIKER, Technol Ctr, 48170 Zamudio, Spain*

Wolfgang J. Parak − *Center for Hybrid Nanostructures (CHyN), Universität Hamburg, 22607 Hamburg, Germany;* orcid.org/0000-0003-1672-6650

Maurizio Prato − *Center for Cooperative Research in Biomaterials (CIC biomaGUNE), Basque Research and Technology Alliance (BRTA), 20014 Donostia, Spain; Ikerbasque, Basque Foundation for Science, 48013 Bilbao, Spain*

Fernando Herranz − *NanoMedMol, Instituto de Química Médica, Consejo Superior de Investigaciones Científicas (IQM-CSIC), Madrid 28006, Spain;* orcid.org/0000-0002-3743-0050

Complete contact information is available at:

https://doi.org/10.1021/acsnano.3c03523
ACS Nano 2023, 17, 13811−13825

https://pubs.acs.org/10.1021/acsnano.3c03523

Author Contributions

[%]L.M.-P. and M.P.-C. contributed equally.

Notes

The authors declare no competing financial interest.

ACKNOWLEDGMENTS

We acknowledge M. Spuch for his scientific drawings and the Basque Government for the R&D Project in Health (grant number 2022333041). S.C.R. acknowledges the Spanish Ministerio de Ciencia e Innovación (MCIN)/Agencia Estatal de Investigación (AEI) Grant PID2019-106139RA-100 funded by MCIN/AEI/10.13039/501100011033 and the Ramon y Cajal Grant RYC2020-030241-I. C.S.C. acknowledges financial support from the Spanish State Research Agency (grant PID2020-118176RJ-I100), and the Gipuzkoa Foru Aldundia (Gipuzkoa Fellows program; grant number 2019-FELL-000018-01/62/2019). This work was performed under the Severo Ochoa Centers of Excellence Program of the Spanish State Research Agency − Grant No. CEX2018-000867-S (DIPC). SXRF analysis was carried out with the support of Diamond Light Source, beamline I18 (proposal SP27720). J.R.C. is funded by MCIN/AEI/10.13039/501100011033 (PID2021-123238OB-I00) and from La Caixa Foundation (Health Research Call 2020: HR20-00075). A.M.G. and C.U. acknowledge the Spanish Ministerio de Ciencia e Innovación (MCIN)/Agencia Estatal de Investigación (AEI) Grant: PID2021-122504NB-I00 funded by MCIN/AEI/10.13039/501100011033 and by "ERDF A way of making Europe. W.J.P. acknowledges funding from the Cluster of Excellence "Advanced Imaging of Matter" of the Deutsche Forschungsgemeinschaft (DFG) - EXC 2056 - project ID 390715994. F.H. acknowledges MCIN (PID2019-104059RB-I00) and M.J.S.G. the Spanish Ministerio de Educación y Formación Profesional (PRE2018-083691).

REFERENCES

(1) Libby, P. The changing landscape of atherosclerosis. *Nature* **2021**, *592*, 524−533.

(2) Libby, P.; Buring, J. E.; Badimon, L.; Hansson, G. K.; Deanfield, J.; Bittencourt, M. S.; Tokgözoğlu, L.; Lewis, E. F. Atherosclerosis. *Nat. Rev. Dis. Primers* **2019**, *5*, 56.

(3) Lusis, A. J. Atherosclerosis. *Nature* **2000**, *407*, 233−241.

(4) Mulder, W. J.; Jaffer, F. A.; Fayad, Z. A.; Nahrendorf, M. Imaging and Nanomedicine in Inflammatory Atherosclerosis. *Sci. Transl. Med.* **2014**, *6*, 239sr1.

(5) Vigne, J.; Thackeray, J.; Essers, J.; Makowski, M.; Varasteh, Z.; Curaj, A.; Karlas, A.; Canet-Soulas, E.; Mulder, W.; Kiessling, F.; Schäfers, M.; Botnar, R.; Wildgruber, M.; Hyafil, F. Cardiovascular study group of the European Society of Molecular, Current and Emerging Preclinical Approaches for Imaging-Based Characterization of Atherosclerosis. *Mol. Imaging Biol.* **2018**, *20*, 869−887.

(6) Carregal-Romero, S.; Miguel-Coello, A. B.; Martínez-Parra, L.; Martí-Mateo, Y.; Hernansanz-Agustín, P.; Fernández-Afonso, Y.; Plaza-García, S.; Gutiérrez, L.; Muñoz-Hernández, M. d. M.; Carrillo-Romero, J.; Piñol-Cancer, M.; Lecante, P.; Blasco-Iturri, Z.; Fadón, L.; Almansa-García, A. C.; Möller, M.; Otaegui, D.; Enríquez, J. A.; Groult, H.; Ruíz-Cabello, J. Ultrasmall Manganese Ferrites for In Vivo Catalase Mimicking Activity and Multimodal Bioimaging. *Small* **2022**, *18*, 2106570.

(7) Ximendes, E.; Benayas, A.; Jaque, D.; Marin, R. Quo Vadis, Nanoparticle-Enabled *In Vivo* Fluorescence Imaging? *ACS Nano* **2021**, *15*, 1917−1941.

(8) Pellico, J.; Lechuga-Vieco, A. V.; Almarza, E.; Hidalgo, A.; Mesa-Nuñez, C.; Fernández-Barahona, I.; Quintana, J. A.; Bueren, J.; Enríquez, J. A.; Ruiz-Cabello, J.; Herranz, F. *In Vivo* Imaging of Lung Inflammation with Neutrophil-Specific ^{68}Ga Nano-Radiotracer. *Sci. Rep.* **2017**, *7*, 13242.

(9) Dong, Y. C.; Hajfathalian, M.; Maidment, P. S. N.; Hsu, J. C.; Naha, P. C.; Si-Mohamed, S.; Breuilly, M.; Kim, J.; Chhour, P.; Douek, P.; Litt, H. I.; Cormode, D. P. Effect of Gold Nanoparticle Size on Their Properties as Contrast Agents for Computed Tomography. *Sci. Rep.* **2019**, *9*, 14912.

(10) Zhang, M.; Xie, Z.; Long, H.; Ren, K.; Hou, L.; Wang, Y.; Xu, X.; Lei, W.; Yang, Z.; Ahmed, S.; Zhang, H.; Zhao, G. Current Advances in the Imaging of Atherosclerotic Vulnerable Plaque Using Nanoparticles. *Mater. Today Bio.* **2022**, *14*, 100236.

(11) Lobatto, M. E.; Calcagno, C.; Millon, A.; Senders, M. L.; Fay, F.; Robson, P. M.; Ramachandran, S.; Binderup, T.; Paridaans, M. P.; Sensarn, S.; Rogalla, S.; Gordon, R. E.; Cardoso, L.; Storm, G.; Metselaar, J. M.; Contag, C. H.; Stroes, E. S.; Fayad, Z. A.; Mulder, W. J. Atherosclerotic Plaque Targeting Mechanism of Long-Circulating Nanoparticles Established by Multimodal Imaging. *ACS Nano* **2015**, *9*, 1837−47.

(12) Sanchez-Gaytan, B. L.; Fay, F.; Lobatto, M. E.; Tang, J.; Ouimet, M.; Kim, Y.; van der Staay, S. E. M.; van Rijs, S. M.; Priem, B.; Zhang, L.; Fisher, E. A.; Moore, K. J.; Langer, R.; Fayad, Z. A.; Mulder, W. J. M. HDL-Mimetic PLGA Nanoparticle to Target Atherosclerosis Plaque Macrophages. *Bioconjugate Chem.* **2015**, *26*, 443−451.

(13) Yin, T.; Li, Y.; Ren, Y.; Fuad, A. R. M.; Hu, F.; Du, R.; Wang, Y.; Wang, G.; Wang, Y. Phagocytosis of Polymeric Nanoparticles Aided Activation of Macrophages to Increase Atherosclerotic Plaques in ApoE−/− Mice. *J. Nanobiotechnol.* **2021**, *19*, 121.

(14) Yahagi, K.; Kolodgie, F. D.; Otsuka, F.; Finn, A. V.; Davis, H. R.; Joner, M.; Virmani, R. Pathophysiology of Native Coronary, Vein Graft, and In-Stent Atherosclerosis. *Nat. Rev. Cardiology* **2016**, *13*, 79−98.

(15) Kim, M.; Sahu, A.; Kim, G. B.; Nam, G. H.; Um, W.; Shin, S. J.; Jeong, Y. Y.; Kim, I. S.; Kim, K.; Kwon, I. C.; Tae, G. Comparison of *In Vivo* Targeting Ability between cRGD and Collagen-Targeting Peptide Conjugated Nano-Carriers for Atherosclerosis. *J. Controlled Release* **2018**, *269*, 337−346.

(16) Pellico, J.; Fernández-Barahona, I.; Ruiz-Cabello, J.; Gutiérrez, L.; Muñoz-Hernando, M.; Sánchez-Guisado, M. J.; Aiestaran-Zelaia, I.; Martínez-Parra, L.; Rodríguez, I.; Bentzon, J.; Herranz, F. HAP-Multitag, a PET and Positive MRI Contrast Nanotracer for the Longitudinal Characterization of Vascular Calcifications in Atherosclerosis. *ACS Appl. Mater. Interfaces* **2021**, *13*, 45279−45290.

(17) Metselaar, J. M.; Lammers, T. Challenges in Nanomedicine Clinical Translation. *Drug delivery Transl. Res.* **2020**, *10*, 721−725.

(18) Niu, Y.-Q.; Liu, J.-H.; Aymonier, C.; Fermani, S.; Kralj, D.; Falini, G.; Zhou, C.-H. Calcium Carbonate: Controlled Synthesis, Surface Functionalization, and Nanostructured Materials. *Chem. Soc. Rev.* **2022**, *51*, 7883−7943.

(19) Rodriguez-Blanco, J. D.; Shaw, S.; Benning, L. G. The Kinetics and Mechanisms of Amorphous Calcium Carbonate (ACC) Crystallization to Calcite, *via* Vaterite. *Nanoscale* **2011**, *3*, 265−271.

(20) Huang, S.-C.; Naka, K.; Chujo, Y. A Carbonate Controlled-Addition Method for Amorphous Calcium Carbonate Spheres Stabilized by Poly(acrylic acid)s. *Langmuir* **2007**, *23*, 12086−12095.

(21) Jia, X.; Kayitmazer, A. B.; Ahmad, A.; Ramzan, N.; Li, Y.; Xu, Y.; Sun, S. Polyacids for Producing Colloidally Stable Amorphous Calcium Carbonate Clusters in Water. *J. Appl. Polym. Sci.* **2022**, *139*, 51899.

(22) Liang, G.; Cao, L.; Chen, H.; Zhang, Z.; Zhang, S.; Yu, S.; Shen, X.; Kong, J. Ultrasmall Gadolinium Hydrated Carbonate Nanoparticle: an Advanced T_1 MRI Contrast Agent with Large Longitudinal Relaxivity. *J. Mater. Chem. B* **2013**, *1*, 629−638.

(23) Dong, L.; Xu, Y. J.; Sui, C.; Zhao, Y.; Mao, L. B.; Gebauer, D.; Rosenberg, R.; Avaro, J.; Wu, Y.-D.; Gao, H.-L.; Pan, Z.; Wen, H. Q.; Yan, X.; Li, F.; Lu, Y.; Cölfen, H.; Yu, S.-H. Highly Hydrated Paramagnetic Amorphous Calcium Carbonate Nanoclusters as an MRI Contrast Agent. *Nat. Commun.* **2022**, *13*, 5088.

(24) VanderSchee, C. R.; Kuter, D.; Chou, H.; Jackson, B. P.; Mann, K. K.; Bohle, D. S. Addressing K/L-edge Overlap in Elemental Analysis from Micro-X-Ray Fluorescence: Bioimaging of Tungsten and Zinc in Bone Tissue Using Synchrotron radiation and laser ablation inductively coupled plasma mass spectrometry. *Anal. Bioanal. Chem.* **2020**, *412*, 259−265.
(25) Varasteh, Z.; Mohanta, S.; Li, Y.; López Armbruster, N.; Braeuer, M.; Nekolla, S. G.; Habenicht, A.; Sager, H. B.; Raes, G.; Weber, W.; Hernot, S.; Schwaiger, M. Targeting Mannose Receptor Expression on Macrophages in Atherosclerotic Plaques of Apolipoprotein E-knockout Mice Using ^{68}Ga-NOTA-anti-MMR Nanobody: Non-Invasive Imaging of Atherosclerotic Plaques. *EJNMMI Res.* **2019**, *9*, 5.
(26) Chinetti-Gbaguidi, G.; Baron, M.; Bouhlel, M. A.; Vanhoutte, J.; Copin, C.; Sebti, Y.; Derudas, B.; Mayi, T.; Bories, G.; Tailleux, A.; Haulon, S.; Zawadzki, C.; Jude, B.; Staels, B. Human Atherosclerotic Plaque Alternative Macrophages Display Low Cholesterol Handling but High Phagocytosis Because of Distinct Activities of the PPARγ and LXRα Pathways. *Circ. Res.* **2011**, *108*, 985−995.
(27) Moore, K. J.; Tabas, I. Macrophages in the Pathogenesis of Atherosclerosis. *Cell* **2011**, *145*, 341−55.
(28) Chen, P. S.; Toribara, T. Y.; Warner, H. Microdetermination of Phosphorus. *Anal. Chem.* **1956**, *28*, 1756−1758.
(29) Donnelly, F. C.; Purcell-Milton, F.; Framont, V.; Cleary, O.; Dunne, P. W.; Gun'ko, Y. K. Synthesis of $CaCO_3$ Nano- and Micro-Particles by Dry Ice Carbonation. *Chem. Commun.* **2017**, *53*, 6657−6660.
(30) Gunasekaran, S.; Anbalagan, G.; Pandi, S. Raman and Infrared Spectra of Carbonates of Calcite Structure. *J. Raman Spectrosc.* **2006**, *37*, 892−899.
(31) Young, A. M.; Sherpa, A.; Pearson, G.; Schottlander, B.; Waters, D. N. Use of Raman Spectroscopy in the Characterisation of the Acid-Base Reaction in Glass-Ionomer Cements. *Biomaterials* **2000**, *21*, 1971−9.
(32) Lv, J.; Liu, Y.; Liu, S.; Feng, Y. L. J.; Zhou, S. Differentiation of Inks Used for Seals by Confocal Raman Microscopy and Fourier Transform Infrared Microscopy. *Spectroscopy* **2015**, *30*, 36−46.
(33) Liu, X.; Qu, S.; Lu, X.; Ge, X.; Leng, Y. Time-of-Flight Secondary Ion Mass Spectrometry Study on the Distribution of Alendronate Sodium in Drug-Loaded Ultra-High Molecular Weight Polyethylene. *Biomed. Mater. (Bristol, U.K.)* **2009**, *4*, No. 065008.
(34) Aime, S.; Caravan, P. Biodistribution of Gadolinium-Based Contrast Agents, Including Gadolinium Deposition. *J. Magn. Reson.Iimaging* **2009**, *30*, 1259−67.
(35) Wei, H.; Bruns, O. T.; Kaul, M. G.; Hansen, E. C.; Barch, M.; Wiśniowska, A.; Chen, O.; Chen, Y.; Li, N.; Okada, S.; Cordero, J. M.; Heine, M.; Farrar, C. T.; Montana, D. M.; Adam, G.; Ittrich, H.; Jasanoff, A.; Nielsen, P.; Bawendi, M. G. Exceedingly Small Iron Oxide Nanoparticles as Positive MRI Contrast Agents. *Pro. Natl. Acad. Sci.* **2017**, *114*, 2325−2330.
(36) García-Soriano, D.; Amaro, R.; Lafuente-Gómez, N.; Milán-Rois, P.; Somoza, Á.; Navío, C.; Herranz, F.; Gutiérrez, L.; Salas, G. The Influence of Cation Incorporation and Leaching in the Properties of Mn-Doped Nanoparticles for Biomedical Applications. *J. Colloid Interface Sci.* **2020**, *578*, 510−521.
(37) Amiri, H.; Bordonali, L.; Lascialfari, A.; Wan, S.; Monopoli, M. P.; Lynch, I.; Laurent, S.; Mahmoudi, M. Protein Corona Affects the Relaxivity and MRI Contrast Efficiency of Magnetic Nanoparticles. *Nanoscale* **2013**, *5*, 8656−8665.
(38) Ta, H. T.; Li, Z.; Wu, Y.; Cowin, G.; Zhang, S.; Yago, A.; Whittaker, A. K.; Xu, Z. P. Effects of Magnetic Field Strength and Particle Aggregation on Relaxivity of Ultra-Small Dual Contrast Iron Oxide Nanoparticles. *Mater. Res. Express* **2017**, *4*, 116105.
(39) Li, H.; Meade, T. J. Molecular Magnetic Resonance Imaging with Gd(III)-Based Contrast Agents: Challenges and Key Advances. *J. Am. Chem. Soc.* **2019**, *141*, 17025−17041.
(40) Liang, X.; Dempski, R. E.; Burdette, S. C. Zn(2+) at a Cellular Crossroads. *Curr. Opin. Chem. Biol.* **2016**, *31*, 120−5.
(41) Sanford, L.; Carpenter, M. C.; Palmer, A. E. Intracellular Zn^{2+} Transients Modulate Global Gene Expression in Dissociated Rat Hippocampal Neurons. *Sci. Rep.* **2019**, *9*, 9411.
(42) Maret, W. Molecular Aspects of Human Cellular Zinc Homeostasis: Redox Control of Zinc Potentials and Zinc Signals. *Biometals* **2009**, *22*, 149−57.
(43) Liu, C. L.; Zhang, X.; Liu, J.; Wang, Y.; Sukhova, G. K.; Wojtkiewicz, G. R.; Liu, T.; Tang, R.; Achilefu, S. Na(+)-H(+) Exchanger 1 Determines Atherosclerotic Lesion Acidification and Promotes Atherogenesis. *Nat. Commun.* **2019**, *10*, 3978.
(44) Shi, X.; Gao, J.; Lv, Q.; Cai, H.; Wang, F.; Ye, R.; Liu, X. Calcification in Atherosclerotic Plaque Vulnerability: Friend or Foe? *Front. Physiol* **2020**, *11*, 56.
(45) Chin, D. D.; Chowdhuri, S.; Chung, E. J. Calcium-Binding Nanoparticles for Vascular Disease. *Regener. Eng. Transl. Med.* **2019**, *5*, 74−85.
(46) Moore, K. J.; Tabas, I. Macrophages in the Pathogenesis of Atherosclerosis. *Cell* **2011**, *145*, 341−355.
(47) Getz, G. S.; Reardon, C. A. Do the Apoe−/− and Ldlr−/− Mice Yield the Same Insight on Atherogenesis? *Arterioscler., Thromb., Vasc. Biol.* **2016**, *36*, 1734−41.
(48) He, H.; Wang, J.; Yannie, P. J.; Korzun, W. J.; Yang, H.; Ghosh, S. Nanoparticle-Based "Two-Pronged" Approach to Regress Atherosclerosis by Simultaneous Modulation of Cholesterol Influx and Efflux. *Biomaterials* **2020**, *260*, 120333.
(49) Sijbers, J.; Scheunders, P.; Bonnet, N.; Van Dyck, D.; Raman, E. Quantification and Improvement of the Signal-to-Noise Ratio in a Magnetic Resonance Image Acquisition Procedure. *Magn. Reson. Imaging* **1996**, *14*, 1157−1163.
(50) Kim, Y.; Lobatto, M. E.; Kawahara, T.; Lee Chung, B.; Mieszawska, A. J.; Sanchez-Gaytan, B. L.; Fay, F.; Senders, M. L.; Calcagno, C.; Becraft, J.; Tun Saung, M.; Gordon, R. E.; Stroes, E. S. G.; Ma, M.; Farokhzad, O. C.; Fayad, Z. A.; Mulder, W. J. M.; Langer, R. Probing Nanoparticle Translocation Across the Permeable Endothelium in Experimental Atherosclerosis. *Proc. Natl. Acad. Sci. U. S. A.* **2014**, *111*, 1078−1083.
(51) Sanchez-Cano, C.; Alvarez-Puebla, R. A.; Abendroth, J. M.; Beck, T.; Blick, R.; Cao, Y.; Caruso, F.; Chakraborty, I.; Chapman, H. N.; Chen, C.; Cohen, B. E.; Conceição, A. L. C.; Cormode, D. P.; Cui, D.; Dawson, K. A.; Falkenberg, G.; Fan, C.; Feliu, N.; Gao, M.; Gargioni, E.; Glüer, C.-C.; Grüner, F.; et al. X-ray-Based Techniques to Study the Nano−Bio Interface. *ACS Nano* **2021**, *15*, 3754−3807.
(52) Aires, A.; Maestro, D.; Ruiz del Rio, J.; Palanca, A. R.; Lopez-Martinez, E.; Llarena, I.; Geraki, K.; Sanchez-Cano, C.; Villar, A. V.; Cortajarena, A. L. Engineering Multifunctional Metal/Protein Hybrid Nanomaterials as Tools for Therapeutic Intervention and High-Sensitivity Detection. *Chem. Sci.* **2021**, *12*, 2480−2487.
(53) Sanchez-Cano, C.; Romero-Canelón, I.; Yang, Y.; Hands-Portman, I. J.; Bohic, S.; Cloetens, P.; Sadler, P. J. Synchrotron X-Ray Fluorescence Nanoprobe Reveals Target Sites for Organo-Osmium Complex in Human Ovarian Cancer Cells. *Chem. − Eur. J.* **2017**, *23*, 2512−2516.
(54) Lo, M. N.; Damon, L. J.; Wei Tay, J.; Jia, S.; Palmer, A. E. Single-cell Analysis Reveals Multiple Requirements for Zinc in the Mammalian Cell Cycle. *eLife* **2020**, *9*, e51107.
(55) Schindelin, J.; Arganda-Carreras, I.; Frise, E.; Kaynig, V.; Longair, M.; Pietzsch, T.; Preibisch, S.; Rueden, C.; Saalfeld, S.; Schmid, B.; Tinevez, J.-Y.; White, D. J.; Hartenstein, V.; Eliceiri, K.; Tomancak, P.; Cardona, A. Fiji: an Open-Source Platform for Biological-Image Analysis. *Nat. Methods* **2012**, *9*, 676−682.
(56) Moharram, M. A.; Allam, M. A. Study of the Interaction of Poly(acrylic acid) and Poly(acrylic acid-poly acrylamide) Complex with Bone Powders and Hydroxyapatite by Using TGA and DSC. *J. Appl. Polym. Sci.* **2007**, *105*, 3220−3227.
(57) Coffman, A. A.; Basta-Pljakic, J.; Guerra, R. M.; Ebetino, F. H.; Lundy, M. W.; Majeska, R. J.; Schaffler, M. B. A Bisphosphonate with a Low Hydroxyapatite Binding Affinity Prevents Bone Loss in Mice after Ovariectomy and Reverses Rapidly with Treatment Cessation. *JBMR Plus* **2021**, *5*, e10476.

https://doi.org/10.1021/acsnano.3c03523
ACS Nano 2023, 17, 13811−13825

(58) Lin, T.-J. Predicting Binding Affinities of Nitrogen-Containing Bisphosphonates on Hydroxyapatite Surface by Molecular Dynamics. *Chem. Phys. Lett.* **2019**, *716*, 83−92.
(59) Solé, V. A.; Papillon, E.; Cotte, M.; Walter, P.; Susini, J. A Multiplatform Code for the Analysis of Energy-Dispersive X-ray Fluorescence Spectra. *Spectrochim. Acta, Part B* **2007**, *62*, 63−68.

https://doi.org/10.1021/acsnano.3c03523
ACS Nano 2023, 17, 13811−13825